Journal of Materials Chemistry A

ROYAL SOCIETY OF CHEMISTRY

PAPER

View Article Online
View Journal | View Issue

Cite this: J. Mater. Chem. A, 2024, 12, 15240

Food-waste-derived hydrochar to a low-cost p-type semiconducting photocatalyst (Zn–Al@HC): multifunctional role in real wastewater treatment and environmental sustainability†

Shraddha Yadav,[a] Monali Priyadarshini,[a] Azhan Ahmad,[b] Makarand M. Ghangrekar *[ab] and Brajesh K. Dubey[b]

The present investigation demonstrates the effectiveness of a novel Zn–Al@HC photocatalyst supported by anaerobically digested food waste-derived hydrochar (HC) for the photocatalytic activation of peroxydisulphate (PDS) and abatement of salicylic acid (SA) in the UV/PDS/Zn–Al@HC system. The morphological and photo-electrochemical characterization of Zn–Al@HC supported the formation of $ZnAl_2O_4$ crystals and the contraction of band gap energy from 3.80 eV ($ZnAl_2O_4$) to 2.36 eV (Zn–Al@HC) by the inclusion of HC (1.86 eV) as a carbon-based support material. Moreover, a remarkable reduction in recombination of photogenerated e^-/h^+ was witnessed in response to UV irradiation in the UV/PDS/Zn–Al@HC system for SA degradation. Under optimal operating conditions, the proposed treatment system achieved 94.45 ± 0.65% degradation of SA. Furthermore, the radical scavenging test revealed the dominance of hydroxyl radical followed by sulphate radicals in the UV/PDS/Zn–Al@HC system, and a potential mechanism was deduced. Cyclic voltammetry for 20 repetitive cycles in a harsh medium affirms the photo-stability of Zn–Al@HC, even under real environmental conditions. The energy-economic valuation of the as-synthesized photocatalyst unveiled the total operating cost and electrical energy per order of UV/PDS/Zn–Al@HC to be 0.1536 $ per m^{-3} $order^{-1}$ and 0.0130 kW h m^{-3} $order^{-1}$, respectively. Thus, the system proves to be a sustainable and economical option for the management of waste and remediation of chemicals of emerging concern, which can be implemented as future large-scale technology for wastewater treatment.

Received 20th January 2024
Accepted 11th March 2024

DOI: 10.1039/d4ta00460d

rsc.li/materials-a

1. Introduction

Salicylic acid (SA) is a chemical of emerging concern (CEC) that is widely used as a raw material in the manufacturing of cosmetics, analgesics, antipyretics, anti-inflammatory drugs such as aspirin, painkillers, and other drugs. Recalcitrant organic SA is highly toxic, endocrine disrupting, non-biodegradable, and bioaccumulates in nature; hence, wastewater containing SA needs to be treated before being discharged into the aquatic system.[1,2] Recently, the photocatalysis-based advanced oxidation process (AOP) has received significant attention for CEC remediation because of its non-toxicity, low cost, better performance, complete mineralization, high stability, and potential for utilizing solar energy.[3,4] The mechanism of photocatalytic degradation involves two stages, including the onsite generation of free radicals (either hydroxyl ($^{\bullet}OH$) or sulphate ($SO_4^{\bullet-}$)) and the reaction of generated radicals with target contaminants leading to their partial or complete mineralisation.[5] However, $SO_4^{\bullet-}$-based AOPs are dominating the present research area as the standard redox potential of $SO_4^{\bullet-}$ (2.5–3.1 eV) is higher than that of $^{\bullet}OH$ (1.9–2.7 eV), it has a longer half-life, can non-selectively target the organic pollutants, and $SO_4^{\bullet-}$-based AOPs are more compatible in a wider pH range.[6] These radicals can be generated *via* the activation of either peroxydisulphate (PDS) or peroxymonosulphate (PMS). The most environment-friendly approach for persulphate activation is UV irradiation, which directly breaks down the chemical bonds of contaminants. Furthermore, UV light can also aid the disintegration of peroxide bonds in the oxidants, which releases free radicals for contaminant degradation.[7]

The heterogeneous semiconductor catalyst ZnO is prominently used to assist the photodegradation process due to its low cost and similar photocatalytic activity to the well-established TiO_2 photocatalyst.[8] Moreover, ZnO possesses a broad energy band gap of 3.4 eV with a high exciton binding

[a]School of Environmental Science and Engineering, Indian Institute of Technology Kharagpur, Kharagpur 721302, India. E-mail: ghangrekar@civil.iitkgp.ac.in

[b]Department of Civil Engineering, Indian Institute of Technology Kharagpur, Kharagpur 721302, India

† Electronic supplementary information (ESI) available. See DOI: https://doi.org/10.1039/d4ta00460d

energy (approx. 60 meV), making it suitable for absorbing UV irradiation as well as high-energy photons.[9,10] However, the high resistivity of ZnO, low visible light absorption (compared to UV), and faster recombination of photogenerated electrons and holes (e^-–h^+) are responsible for its limited application. The optical and photocatalytic properties of ZnO can be upgraded by incorporating a group III element, *e.g.*, aluminium (Al), which is non-toxic, thermally stable, brings changes in lattice parameters, and induces surface structural defects. Generally, the surface defects improve the photocatalytic activity owing to the reduction in the recombination of charge carriers.[11]

Furthermore, the e^-–h^+ recombination can be retarded by the construction of heterojunction composites using organic and inorganic materials, which facilitate PDS activation *via* direct e^- transfer. For instance, heterojunction photocatalysts PDINH/MIL-88A(Fe) and $Fe_3(PO_4)_2 \cdot 8H_2O$ (vivianite) were reported to effectively activate PDS through a similar synergistic effect and therefore, successfully participated in CEC elimination.[12,13] In this direction, incorporation of a carbon-based support material such as hydrochar (HC) provides better stability and recyclability to the semiconductor-based photocatalysts.[14] Compared to commercially available carbon materials, *i.e.*, activated carbon or biochar (BC), the synthesis of HC is less energy intensive and it is compatible with moisture-containing precursors (*e.g.*, digestate) as well. Moreover, the HC-based catalyst was also reported to have a significant impact on oxidant (such as PDS, PMS) and hydrogen peroxide (H_2O_2) activation to generate reactive radicals in AOPs.[15] As a step towards an economic and sustainable catalyst synthesis, researchers are utilizing sludge/digestate as the precursor for HC. For instance, Wei and the co-researcher utilized iron-modified sewage sludge-derived HC as a catalyst for PDS activation and achieved 99.72% degradation efficiency for tetracycline (antibiotic).

To the extent of our understanding, this is the first investigation that utilised anaerobically digested food waste (AD-FW) derived HC modified with Zn–Al precursor for the synthesis of a photocatalyst (Zn–Al@HC). Further, its application in a UV/PDS system for SA degradation has been demonstrated. The detailed characterization (morphological, structural, optical, and photo-electrochemical) of Zn–Al@HC and optimization of operating parameters were performed. Furthermore, the effect of anions, versatile aqueous matrix, and catalytic mechanism during the UV/PDS/Zn–Al@HC process, and the mineralisation pathway for SA degradation are also proposed based on the radical scavenging experiments. Importantly, the energy-cost analysis emphasizes the potential of Zn–Al@HC as a low-cost, highly efficacious, and sustainable photocatalyst for SA degradation in the future.

2. Experimental analysis

2.1. Reagents, chemicals, and Zn–Al@HC synthesis approach

For the present investigation, chemicals such as sodium persulphate ($Na_2S_2O_8$), sodium chloride (NaCl), sodium fluoride (NaF), sodium phosphate (Na_3PO_4), sodium carbonate (Na_2CO_3), sodium nitrate ($NaNO_3$), zinc oxide (ZnO), and aluminium oxide (Al_2O_3) of laboratory grade were procured from Merck, India, whereas SA was procured from Sigma Aldrich ($C_7H_6O_3$, >99% pure). Additional reagents used during the experiments were *tert*-butyl alcohol (TBA; $C_4H_{10}O$, Advent Chembio Pvt. Ltd, 99%), *p*-benzoquinone (BQ; ≥99.5%), methanol (MeOH; CH_3OH, Merck, 99%), 5,5-dimethyl-1-pyrroline N-oxide (DMPO, Sigma Aldrich, >99%), and ethylenediaminetetraacetate disodium salt dihydrate (Na_2-EDTA; 99%). Carbon tetrachloride (CCl_4, 99%) was procured from Universal Fine Chemicals, India. The photocatalyst was synthesized using the co-precipitation technique[16] from the anaerobic digestate of food waste, as described further in Text S1.†

2.2. Physicochemical, morphological, and electrochemical characterization

Pristine HC (210 °C, 4 h) and the photocatalyst Zn–Al@HC (210 °C, 4 h) were characterized for physicochemical and morphological characteristics as described in detail (Text S2†). Furthermore, the absorption bands and photocatalytic activity of the prepared novel catalyst were determined using the UV-vis diffuse reflectance spectra (DRS) and chronoamperometry (CA). Photoluminescence (PL) spectroscopy was carried out using a fluorescence spectrophotometer (Cary Eclipse, Agilent Technologies, USA) to analyse the charge carrier separation efficacy of the as-synthesized catalyst. The PL spectroscopy was conducted in the wavelength range of 200 nm to 600 nm with an excitation wavelength of 350 nm at ambient temperature. A similar protocol for the PL characterization was followed by Li *et al.* and Ghosh *et al.*[17,18] Additional electrochemical analysis including Cyclic Voltammetry (CV), Linear Sweep Voltammetry (LSV), Mott–Schottky (M–S) analysis, and Electrochemical Impedance Spectroscopy (EIS) were conducted both under UV irradiation and in the dark to determine the photocurrent response.

2.3. UV/PDS/Zn–Al@HC photocatalytic degradation and optimization

Photocatalytic degradation experiments was conducted as per the method mentioned in Text S3.† After 30 min of the initial adsorption test, the system was exposed to a source of UV radiation (11 W, Phillips, India) for 120 min. The sample was collected at regular intervals of 20 min and monitored using a UV-visible spectrophotometer at a wavelength of 297 nm.[19] The UV/PDS/Zn–Al@HC photocatalytic degradation was performed to investigate the effect of different anions, including chloride (Cl^-), nitrate (NO_3^-), fluoride (F^-), carbonate (CO_3^{2-}), and phosphate (PO_4^{3-}) at variable concentrations, *i.e.*, 0 to 15 mM. Later, a comparative analysis of the SA degradation efficiency in three different water matrices, *i.e.*, distilled water, tap water, and wastewater treatment plant (WWTP) effluent (procured from the Indian Institute of Technology campus, Kharagpur, West Bengal, India) was performed and evaluated under the optimized conditions to affirm its real field scalability. Furthermore, the residual sulphate and metal ion

concentration in the final UV/PDS/Zn–Al@HC effluent was determined using Ion Chromatography (IC, Eco-IC, Metrohm, Switzerland) to assess the downstream potent hazards of the UV/PDS/Zn–Al@HC effluent.

2.4. Toxicity and reusability evaluation

To determine the toxic effects of untreated SA samples and UV/PDS/Zn–Al@HC treated SA samples, phytotoxicity assessment on *Vigna radiata* was conducted. The assessment was performed in a Petri dish where five seeds were sown and watered (5 ml each day) for twelve days with both treated and untreated water separately. The results were evaluated in terms of root and shoot length on the last day. Furthermore, Zn–Al@HC was recovered using a vacuum filtration process from the treated effluent of the UV/PDS/Zn–Al@HC system and dried in an oven at 60 °C to evaluate the reusability capacity (conducted in triplicate) of the as-synthesised catalyst.

3. Results and discussion

3.1. Morpho-chemical characterization and properties of Zn–Al@HC

The scanning electron microscopy (SEM) micrograph of the pristine HC derived from AD-FW revealed the existence of fibrous and highly porous skeleton-like morphology (Fig. 1a). The porosity of the HC verified its ability to function as the best support material for the Zn–Al composite. However, the texture of pristine HC was destroyed after Zn–Al activation and resulted in more porous microspheres in the Zn–Al@HC. Moreover, the SEM images of Zn–Al@HC showed the appearance of white ultrafine particulates of $ZnAl_2O_4$ on the surface of HC and a great effect on the textural properties of the HC (Fig. 1b).[20] The cross-linking between the small microspheres to form large microspheres suggests the better occurrence of polymerization and condensation reaction during the HTC of AD-FW in the presence of Zn–Al.[21] Additionally, it supports the harvesting of UV irradiation due to increased surface area and multiple scattering of light within the porous framework. Furthermore, the elemental composition was assessed using Energy Dispersive Spectroscopy (EDS), which revealed the uniform distribution of each element within the Zn–Al@HC photocatalyst (Fig. 1c).

The Fourier transform infrared spectroscopy (FTIR) spectra of pristine HC and Zn–Al@HC have been presented in Fig. 2a, which suggested the dominance of the oxygen functional groups, such as aromatic C=O stretching of conjugated quinones and ketones in the wavelength between 1500 cm^{-1} and 1600 cm^{-1}. Both the samples exhibited common broad bands between 3699 cm^{-1} and 2920 cm^{-1} due to the –OH stretching of the interlayer water molecule. The formation of a hydrogen bond is responsible for the broadening of the band. However, the absence of –OH stretching mode in Zn–Al@HC represented the hydrophobic nature of the prepared photocatalyst Zn–Al@HC.[22] The original structure of HC remains intact after Zn–Al@HC composite formation. In the FTIR spectra, the bands around 560 cm^{-1} and 680 cm^{-1} represent the vibration of Zn–O bonds at the tetrahedral site, whereas the small peaks around 505 cm^{-1} could be attributed to the Al–O bonds in the octahedral site of the $ZnAl_2O_4$ spinel.[23] The visible band around 700–450 cm^{-1} can be related to the lattice vibration modes of O–Zn–O.[24]

The X-ray diffraction (XRD) characterization of the pristine HC and as-synthesized Zn–Al@HC photocatalyst is represented

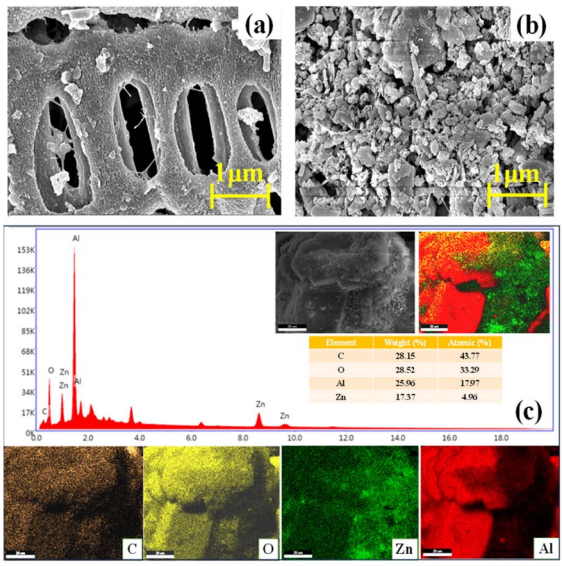

Fig. 1 (a and b) SEM interpretation of pristine HC and the as-synthesized Zn–Al@HC photocatalyst, (c) EDS spectrum of Zn–Al@HC (with the corresponding elemental mapping of C, O, Zn, and Al, respectively).

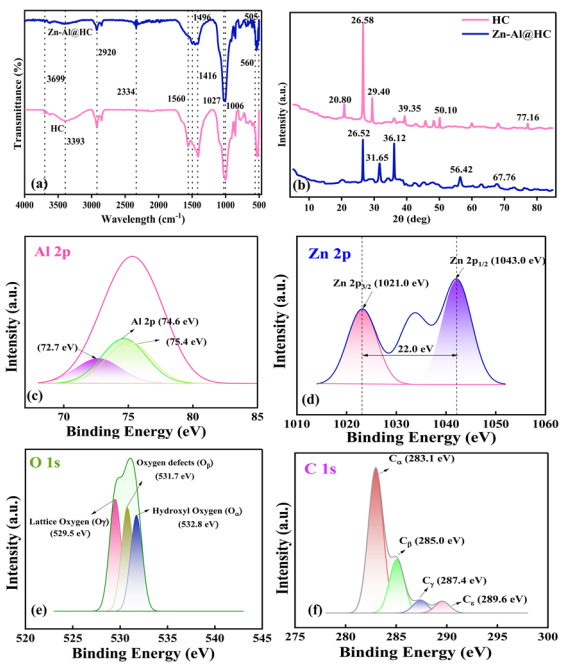

Fig. 2 (a) FTIR, (b) XRD of pristine HC and the Zn–Al@HC photocatalyst, and (c–f) XPS spectra of the Zn–Al@HC photo-catalyst (Al 2p, Zn 2p, C 1s, O 1s).

in Fig. 2b. In accordance with the XRD pattern, differentiated peaks (2θ) at 20.80°, 26.58°, 29.40°, 39.35°, 50.10°, and 77.16° were evident for the pristine HC. The presence of peaks between 10° and 35° reflects the amorphous nature of the carbon-based support material.[25] Interestingly, the diffraction peak around 26.5° in both HC and Zn–Al@HC showed a high degree of graphitization. However, the peaks at 20.8° and 29.40° correspond to inorganic impurities SiO_2 and $CaCO_3$ in the pristine HC, which were absent after Zn–Al activation of HC.[26] Furthermore, a decrease in the intensity of the SiO_2 peak was observed with the addition of the Zn–Al composite during the synthesis, which might be due to carbon gradually covering the crystal plane of SiO_2.[27]

For the synthesized Zn–Al@HC photocatalyst, the XRD pattern obtained at 31.65° [220], 36.12° [311], and 56.42° [422], (JCPDS no: 00-005-0669) affirmed the formation of $ZnAl_2O_4$ spinel phase in the photocatalyst supported by the carbonaceous structure, which follows the previous investigation conducted on the BC-$ZnAl_2O_4$ composite[28] and Zn/Al LDHs@C.[29] Note that the decrease in crystallization degree and improvement in the amorphous sites in the Zn–Al@HC photocatalyst can cause structural defects and impact both the photo-induced e^-/h^+ pairs and the efficiency of resulting charge carrier separation. This phenomenon will be further supported by CA and EIS results in the following sections.

X-ray Photoelectron Spectroscopy (XPS) was carried out to further confirm the elemental concoction and surface electronic state of Zn–Al@HC. The XPS region of Al 2p is located in the range of 72–75 eV (Fig. 2c), which illustrates the presence of Al^{3+} on the plane of the photocatalyst. As per the literature, the Al 2p peak corresponds to Al^{3+}, *i.e.*, aluminium with oxidation number 3+. Also, the results were consistent with the assigned peak of 74.3 eV in Fe_2O_3/Zn–Al LDH by Li *et al.* (2020).[30] Moreover, the Zn 2p spectrum (Fig. 2d) of Zn–Al@HC at 1021.0 eV and 1043.0 eV belongs to the two components Zn $2p_{1/2}$ and Zn $2p_{3/2}$, respectively, due to spin–orbit splitting. The difference in binding energies between these components is 22 eV, which supports the XRD results of $ZnAl_2O_4$ formation in the synthesized composite and a clear transition from Zn to Zn^{2+} state of the metal.[9,31]

Herein, from Fig. 2e, four C peaks were observed, which could be attributed to the oxygen-based functional groups of the HC-based photocatalyst (Zn–Al@HC). The XPS spectrum of C_α at 283.1 eV corresponds to two-coordinated carbon atoms (such as aliphatic/aromatic carbon groups; C–H, C–C).[32] Furthermore, the peaks at 285.0 eV (C_β), 287.4 eV (C_γ), and 289.6 eV (C_ε) reflect the presence of hydroxyl/ether/C–O, quinone/carbonyl/C=O, and carboxylic/ester/O– C=O groups. Additionally, C_β affirms the presence of C in a graphitic environment, whereas the deconvolution at C_γ supports the formation of C–N bonds in the synthesized photocatalyst.[33] Both graphitic C and C–N are responsible for enhanced photocatalytic activity due to improved charge absorption properties and the synergy between their crystallographic and electronic structure.[34]

The high resolution spectra of O 1s in Zn–Al@HC are evident in Fig. 2f and are fitted into three peaks at 529.5 eV, 531.7 eV, and 532.8 eV, which correspond to lattice oxygen (O_γ), oxygen defects (O_β), and adsorbed water molecules on the surface (O_α).[35] The cumulative effects of the chemical bonding state and photogenerated e^- transfer are responsible for the outstanding photocatalytic properties of the synthesized Zn–Al@HC. Moreover, Brunauer–Emmet–Teller (BET) surface analysis (BEL, Japan, Inc.) demonstrated a surface area of 19.51 $m^2\ g^{-1}$ and pore volume of 0.032 $cm^3\ g^{-1}$ of the as-synthesized Zn–Al@HC catalyst, which are relatively higher than those of the HC (14.27 $m^2\ g^{-1}$, 0.016 $cm^3\ g^{-1}$). In addition, the adsorption–desorption curves of both HC and Zn–Al@HC exhibit a Type IV isotherm (Fig. S1a and b†) with an H3 hysteresis loop and a pore radius of 4.57 nm and 1.57 nm, which mainly suggest the existence of a mesoporous structure with capillary condensation that tentatively contributes to radical generation by activating PDS in the UV/PDS/Zn–Al@HC system.[36]

3.2. Photoelectrochemical characterization and stability of Zn–Al@HC

3.2.1. UV-vis diffuse reflectance spectra (DRS) (Kubelka–Munk's plot). UV-vis DRS was performed to evaluate the optical properties of the synthesized photocatalyst Zn–Al@HC. The photocatalytic reactions are highly dependent on the light absorption by the material and the migration of light-induced e^-–h^+.[37] The strong absorption band in the UV-visible region for pristine HC is visible in Fig. 3a, while Zn–Al@HC has a strong absorption band illustrating bathochromic shifts

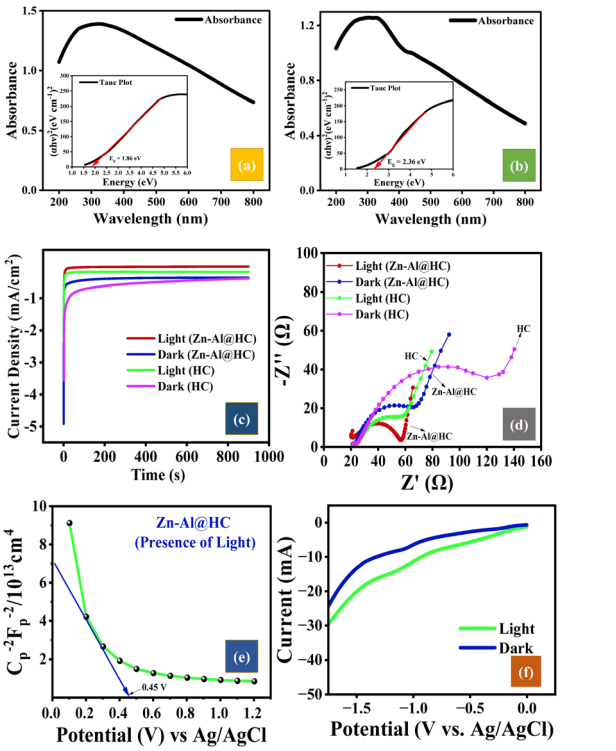

Fig. 3 (a and b) UV-DRS of pristine HC and Zn–Al@HC, (c) chronoamperometric analysis of HC and Zn–Al@HC (UV illuminated and dark system), (d) Nyquist plot for HC and Zn–Al@HC under UV and dark conditions, and (e) Mott–Schottky plot under UV light, (f) LSV curves under UV illuminated and dark conditions.

compared to HC Fig. 3b. The absorption edge of Zn–Al@HC is located at approximately 370 nm in line with the previously reported value of 390 nm by Ramani *et al.* and Suwanboon *et al.* for zinc oxide and g-C_3N_4/$ZnAl_2O_4$ nanoparticles, respectively.[38,39] This result indicates the prominent optical properties of Zn–Al@HC in the UV region.[40]

The energy band gap value (E_g) of the sample was estimated from extrapolation of the Tauc plot of $(\alpha hv)^2$ *vs.* photon energy (hv) to zero based on the Kubelka–Munk formula (eqn (1)).

$$(\alpha hv) = A(hv - E_g)^{n/2} \quad (1)$$

where α is the absorption coefficient (6.626×10^{-34} J s), h is Plank's constant, v is the frequency of light, A is the band tailing parameter, and n is the optical transition coefficient, respectively.

As per the literature, ZnO, Al_2O_3, and $ZnAl_2O_4$ have wide energy band gaps of 3.4 eV, 7.1 eV, and 3.8 eV, respectively,[41] which were significantly reduced by the doping of Zn–Al on the HC surface having a band gap of 1.86 eV (Fig. 3a). The resultant band gap of the synthesized composite Zn–Al@HC was found to be 2.36 eV (Fig. 3b) and predicted to exhibit enhanced photocatalytic activity. The results were similar to those obtained in the ZnO–BC composite photocatalyst having a band gap of 2.97 eV, higher than that of pristine BC (1.52 eV) but lower than that of ZnO (3.06 eV). The ZnO–BC photocatalyst was reported to achieve 98.5% degradation of ciprofloxacin in 240 min.[42]

The reduction in the band gap of Zn–Al@HC as compared to $ZnAl_2O_4$ might be due to the structural defects (as affirmed by FTIR and XPS analysis) and interaction with the carbon content of HC. Structural defects improved the interaction of the electric surface charge of metal oxides in the Zn–Al@HC composite and modified the e^-–h^+ separation process or radical generation under UV irradiation.[42] Thus, the synthesized composite has a better ability to absorb more UV-visible light, which enhances the photocatalytic degradation of SA. Similarly, other HC-based photocatalysts have been reported to effectively degrade emerging contaminants as shown in Table S1.†

3.2.2. Photo-induced chronoamperometry. Chronoamperometry analysis for both pristine HC and as-synthesized Zn–Al@HC was conducted in a typical three-electrode system for 960 s and at an applied potential of −1 V. The trends of photocurrent obtained under both UV illumination and dark conditions are presented in Fig. 3c. The chronoamperometric inferences are consistent with the EIS results, representing the better stability and photocurrent density of Zn–Al@HC compared to HC. The photocurrent plots for Zn–Al@HC and HC illustrated an average photocurrent density of −0.15 mA cm^{-2} and −0.58 mA cm^{-2}. Additionally, the photocurrent density decreases nearly 5.6 times in the dark conditions. Furthermore, the photocurrent response of Zn–Al@HC under UV illumination remained more stable and reversible for a longer duration. This might be attributed to the activation of Zn–Al@HC in the presence of UV irradiation to produce e^-–h^+ charge carriers and lower e^-–h^+ recombination.[43] Thus, Zn–Al@HC proved to be a highly potent photocatalyst for contaminant degradation under UV exposure.

3.2.3. Nyquist plots. To investigate the charge transfer resistance of the photocatalyst, EIS was conducted. As stipulated in Nyquist plots (Fig. 3d), the semicircle arc of Zn–Al@HC (under light exposure conditions) is smaller as compared to that in the dark and pristine HC. The Nyquist plots also corroborate the formation of a heterojunction and reduce the resistance for charge carrier migration in the Zn–Al@HC photocatalyst as compared to the pristine HC. Additionally, a remarkable reduction in the recombination of photogenerated e^-/h^+ was witnessed in response to UV irradiation in the UV/PDS/Zn–Al@HC system for SA degradation. The UV-DRS analysis affirmed the formation of a heterojunction between HC and Zn–Al composite and lessened the resistance for charge carrier migration and the analogous recombination rate.[44]

3.2.4. Mott–Schottky (M–S) analysis. The M–S analysis was conducted using 0.05 M Na_2SO_4 solution in the presence of optimum 0.01 M PDS at 1000 Hz frequency in the dark conditions and under a constant AC potential. The M–S analysis is generally carried out to identify the semiconducting nature (*i.e.*, p-type (−ve slope) or n-type (+ve slope)) of the Zn–Al@HC photocatalyst and carrier charge density. Zn–Al@HC shows the −ve (in Fig. 3e) slope confirming the p-type semiconducting properties, which was also supported by Liu *et al.*[45] From the M–S plot, the flat band potential (E_{fb}) of Zn–Al@HC was found to be 0.45 eV *vs.* Ag/AgCl. The E_{fb} at the standard electrode potential of Ag/AgCl ($E^0_{Ag/AgCl}$ ~0.198 eV at 25 °C) was converted to E_{fb} *vs.* normal hydrogen electrode potential (E_{NHE}) using eqn (2). The pH value of Na_2SO_4 and PDS solution was found to be 6.97.

$$E_{NHE} = E_{Ag/AgCl}\,(\text{at pH } 6.9) - 0.059\,(7 - \text{pH of the electrolyte}) + E^0_{Ag/AgCl} \quad (2)$$

For Zn–Al@HC, E_{fb} is found to be equal to 0.646 eV *vs.* NHE from the above eqn (2). Furthermore, to examine the photocatalytic mechanism of Zn–Al@HC, the potential of the valence band (E_{VB}) and conduction band (E_{CB}) should be determined using eqn (3) and (4).

$$E_{VB} = X - E_0 + 0.5E_g \quad (3)$$

$$E_g = E_{VB} - E_{CB} \quad (4)$$

where X is the absolute electronegativity of Zn–Al@HC (~5.34 eV), E_0 is the free e^- energy on the H-scale (~4.50 eV) and E_g is the energy band gap of Zn–Al@HC (~2.36 eV from the Kubelka–Munk plot).

For the as-synthesized photocatalyst, X and E_g are approximately equal to 5.34 eV and 2.36 eV. Thus, the calculated E_{VB} and E_{CB} for Zn–Al@HC are about 2.02 eV and −0.34 eV, respectively. As per the literature, the potential for superoxide radicals $O_2^{\bullet-}/O_2$ is −0.33 eV *vs.* NHE, $^{\bullet}OH/H_2O$ is +1.99 eV *vs.* NHE, and $^{\bullet}OH/OH^-$ is +2.40 eV *vs.* NHE.[46] The E_{CB} for Zn–Al@HC is −0.34 eV, which is more negative than the $O_2^{\bullet-}/O_2$ potential, therefore, the UV/PDS/Zn–Al@HC system has greater tendency towards the generation of $O_2^{\bullet-}$, which might later transform into $^{\bullet}OH$.[47] Additionally, the photogenerated h^+ of E_{VB} are sufficient to perform either the photolysis of H_2O_2 by 2

e^- reduction of O_2 (*i.e.*, $O_2/H_2O_2 \sim +0.682$ eV) or oxidation of hydroxyl ion (OH^-) and H_2O to generate $^{\bullet}OH$ (*i.e.*, $^{\bullet}OH/H_2O \sim +1.99$ eV, $OH^-/H_2O \sim +1.23$ eV) imperative to the formation of $^{\bullet}OH$.[48] Moreover, the photocatalyst has the oxidative selectivity to produce H_2O_2 ($H_2O_2/H_2O \sim +1.76$ eV) and further release $^{\bullet}OH$ ($H_2O_2/^{\bullet}OH \sim +0.73$ eV).[49,50] Hence, the UV/PDS/Zn–Al@HC system has both the active species $O_2^{\bullet-}$ and $^{\bullet}OH$ besides the photogenerated holes. The domination of $^{\bullet}OH$ was also established *via* a radical scavenging experiment, therefore corroborating with the aforementioned hypothesis, which is elaborated in Section 3.6. Another co-existent radical is PDS ($S_2O_8^{2-}/S_2O_8^{\bullet-}$) having a redox potential of +2.01 eV, however, it is incapable of producing $SO_4^{\bullet-}$ (2.5–3.1 eV) directly.[51]

3.2.5. Electrochemical/voltammetry analysis. Additionally, CV and LSV were also executed under UV illumination and the dark condition for the synthesized photocatalyst (Zn–Al@HC). The analyses were performed at a scan rate of 0.05 V s^{-1} in the presence of 50 mM Na_2SO_4 electrolyte with platinum and Ag/AgCl as counter and reference electrodes, respectively. As stipulated in LSV curves (Fig. 3f), Zn–Al@HC showed lower response without UV, whereas it manifested a higher cathodic photocurrent of 30.12 mA (1.3 times higher) in the presence of UV. The electrochemical evaluation of the as-synthesized catalysts for photocatalytic activity indicated the easier charge migration in Zn–Al@HC, thereby greatly enhancing the photogenerated e^-–h^+ in the conduction and valence bands.

Furthermore, after 20 cycles of CV under ideal experimental conditions (*i.e.*, in the absence of PDS), the results revealed a much higher and more stable current response of Zn–Al@HC, which affirms its high reusability and recyclability. In addition, profound oxidation and reduction peaks were also observed at 1.5 V and −1.0 V, respectively, which signify the enhanced redox properties of the as-synthesised catalyst (Fig. 4a). On performing the same 20 cycles CV under harsh operating conditions (under 0.01 M PDS, 50 mg L^{-1} SA, 50 mM Na_2SO_4), a current drop of 26.5% was observed under UV-exposed conditions, which was much less compared to that in the dark (Fig. 4b). This is attributed to the high photostability and high photoelectrochemical response of Zn–Al@HC under a UV-exposed system, supporting the results obtained from LSV and CA analysis.

3.2.6. Photoluminescence analysis. From the results of PL spectra (Fig. 5a–d), it was observed that ZnO exhibited a high intensity peak in the UV region at 350.10 nm, whereas Al_2O_3 exhibited a higher peak with a slight wavelength shift in the UV-vis region at 400.39 nm, which shows the lower photocatalytic activity of Al_2O_3. However, the intensity of the peak reduced in the case of $ZnAl_2O_4$ crystals at 400.47 nm, which was minimum in the case of as-synthesized Zn–Al@HC (at 450.91 nm), illustrating the superior photocatalytic properties of the as-synthesized catalyst. This suggests that the added HC may function as an electron trap, allowing the $ZnAl_2O_4$ electrons to be attracted to the HC when exposed to UV light.[52] Furthermore, it speeds up the migration and separation of electron–hole pairs, suppresses the charge-carrier recombination, and increases the effectiveness of Zn–Al@HC for the SA degradation process.[17,53] Furthermore, a red shift as observed in the sub-spectra (Fig. 5a1–d1) emphasizes the compatibility of Zn–Al@HC for visible light simulation, which also extends its applicability for the solar-photo degradation process.

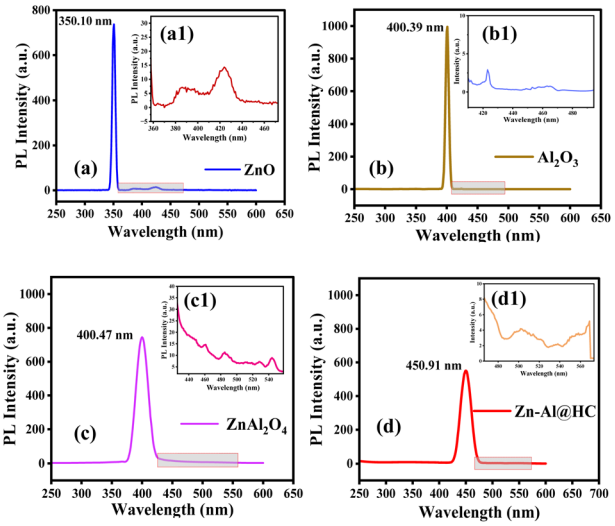

Fig. 5 PL spectra and sub-spectra of (a and a1) pure ZnO, (b and b1) pure Al_2O_3, (c and c1) co-precipitated $ZnAl_2O_4$, (d and d1) and as-synthesized Zn–Al@HC photocatalyst.

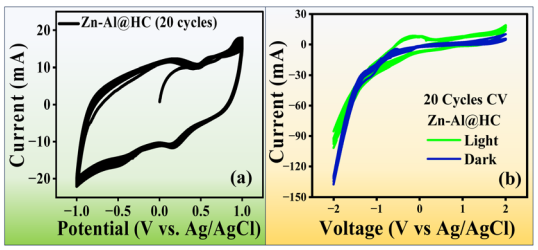

Fig. 4 (a) 20 Cycles CV under ideal operating conditions, (b) 20 cycles CV for Zn–Al@HC (real environmental conditions; both UV illuminated and dark systems).

3.3. UV/PDS/Zn–Al@HC degradation of SA and control experiments

The photocatalytic performance of Zn–Al@HC as the PDS activator in SA degradation was evaluated under UV light. As illustrated in Fig. 6a, the control UV irradiation has minimal SA degradation efficiency, indicating that the contribution of UV light alone is negligible. Meanwhile, SA was barely degraded in 150 min (including 30 min of dark study) in the case of control Zn–Al@HC and control PDS. The negligible degradation in the presence of PDS alone might be due to its limited oxidation potential (2.01 V). Moreover, Zn–Al@HC had a less than 10% (*i.e.*, 9.34 ± 0.32%) efficiency of SA degradation under UV irradiation alone, which might be due to extensive recombination of charge carriers in the case of the pure catalyst. Without UV exposure, Zn–Al@HC and PDS together were unable to degrade SA, manifesting the significance of UV light in the system. Interestingly, an improvement in SA degradation efficiency to

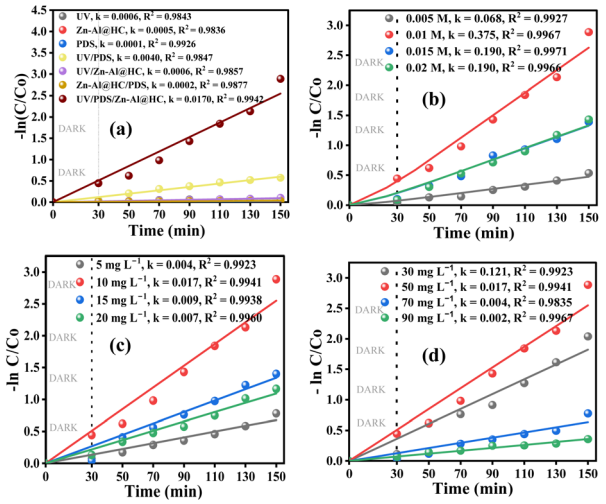

Fig. 6 (a) Photocatalytic degradation of SA and kinetics involved under different (b) PDS dosages, (c) Zn–Al@HC dosages, and (d) pollutant concentrations. (pH_0 of 7.0, temperature of 27 °C, Zn–Al@HC of 10 mg L^{-1}, UV irradiation of 11 μW cm^{-2}, SA concentration of 50 mg L^{-1}, and PDS of 0.01 M.)

43.35 ± 0.15% was observed after the introduction of UV into the PDS system, thus indicating the activation of PDS in the presence of UV light; however, the degradation efficiency is still less than 50% (Fig. S2a†). After exposing the Zn–Al@HC-based photocatalyst to the UV/PDS system, outstanding photocatalytic activity and enhancement in the SA degradation (up to 94.45 ± 0.65%) were noticed. As for the SA solution, the photocatalytic degradation process followed the pseudo-first-order kinetics as indicated in eqn (5).

$$-\ln\frac{C_t}{C_o} = kt \quad (5)$$

where k represents the degradation rate constant (min^{-1}), C_o is the initial concentration of SA (mg L^{-1}), and C_t is the final concentration of the SA after irradiation for time t (min), respectively.

These results emphasized the existence of a synergistic effect between PDS and Zn–Al@HC (PDS activation effect of Zn–Al@HC) under UV light. Additionally, the PDS entrapped the conduction band photoelectrons, prevented e^-–h^+ recombination, and generated $SO_4^{\bullet-}$ and $^{\bullet}OH$ with high oxidizing ability. The mechanism behind the role of Zn–Al@HC in the radical generation is illustrated in eqn (6)–(9).

$$\text{Zn–Al@HC} + h\nu \rightarrow \text{Zn–Al@HC}\ (h^+ + e^-) \quad (6)$$

$$S_2O_8^{2-} + e^- \rightarrow SO_4^{\bullet-} + SO_4^{\bullet-} \quad (7)$$

$$SO_4^{\bullet-} + H_2O \rightarrow {}^{\bullet}OH + SO_4^{2-} + h^+ \quad (8)$$

$$h^+/\ SO_4^{\bullet-}/{}^{\bullet}OH + SA \rightarrow \text{intermediates} \rightarrow CO_2 + H_2O \quad (9)$$

3.3.1. Effect of peroxydisulphate (oxidizer) dosage. In the heterogeneous PDS photocatalytic system, PDS dose is directly correlated with the number of reactive radicals generated. Fig. 6b stipulates the effect of PDS concentration on SA degradation in the UV/PDS/Zn–Al@HC system. On increasing the PDS concentration from 0.005 to 0.01 M, an increment in degradation efficiency from 41.38 ± 0.50% to 94.45 ± 0.65% (Fig. S2b†) was observed under constant Zn–Al@HC (10 mg L^{-1}) and UV conditions. The increment might be due to greater generation of reactive radicals for the higher dose of PDS. However, when PDS dosage was further increased from 0.015 to 0.02 M the SA degradation rate was significantly decreased. For a particular dose of photocatalyst, e^- and h^+ are constant, hence, the excessive PDS concentration might be responsible for the side reactions of PDS with the available $SO_4^{\bullet-}$ radicals (eqn (10) and (11)).[54] These side reactions decrease the number of reactive radicals for the oxidation of SA, therefore the optimal PDS concentration of 0.01 M was selected and used for further experiments.

$$SO_4^{\bullet-} + S_2O_8^{2-} \rightarrow SO_4^{2-} + S_2O_8^{\bullet-} \quad (10)$$

$$SO_4^{\bullet-} + SO_4^{\bullet-} \rightarrow S_2O_8^{2-} \quad (11)$$

3.3.2. Effect of Zn–Al@HC (catalyst) dosage. The effect of Zn–Al@HC dosage on the catalytic degradation of SA (50 mg L^{-1}) in the UV/PDS/Zn–Al@HC system was investigated at 0.01 M PDS dose (Fig. 6c). On decreasing the Zn–Al@HC dosage from 20 mg L^{-1} to 15 mg L^{-1} and 10 mg L^{-1}, an increasing trend in SA degradation efficiency, *i.e.*, 68.81 ± 1.50%, 75.35 ± 1.35%, and 94.45 ± 0.65% was witnessed (Fig. S2c†). This might be due to the agglomeration of particles and high opacity of the aqueous solution at a high concentration of the catalyst, which hinders UV penetration through the solution.[55] However, when the Zn–Al@HC dose was further reduced to 5 mg L^{-1} from 10 mg L^{-1}, the SA removal was drastically decreased to 54.20 ± 0.50% from 94.45 ± 0.65%. The reason for the sudden decrease is attributed to the lack of active sites for PDS activation and SA elimination under a low dosage of Zn–Al@HC.[56]

3.3.3. Effect of initial SA (pollutant) concentration. The effect of the initial concentration of pollutant on the degradation capability of the Zn–Al@HC photocatalyst was evaluated at the optimum catalyst and PDS dose of 10 mg L^{-1} and 0.01 M, respectively. Despite the low concentration of the model pollutant SA found in real wastewater, to check the performance efficiency of the UV/PDS/Zn–Al@HC system, higher concentrations of SA were chosen in this investigation. The results in Fig. S2d† revealed the decrement in degradation efficiency with increasing SA concentration beyond 50 mg L^{-1}. Based on the scenario, the results of Fig. 6d can be interpreted as that at a fixed concentration of Zn–Al@HC, PDS, and irradiation intensity, the number of reactive radicals generated ($SO_4^{\bullet-}$ and $^{\bullet}OH$) at the catalyst surface can be assumed to be constant. Thus, the lower degradation at higher concentrations of SA might be due to the insufficient generation of reactive radicals and the lesser interaction between the reactive species and the pollutant molecules.[57] Also, the availability of large pollutant

molecules interferes with the UV (photons) absorption effectively, thereby resulting in a decrease in degradation efficiency with an increase in the initial concentration of SA.[58] However, examining the degradation efficiency at a concentration of 30 mg L^{-1} also resulted in a slightly lower degradation rate, which might be due to incompetent exposure to radicals with the SA molecule. Thus, 50 mg L^{-1} can be considered the optimal SA concentration for the effective working of the catalyst in the UV/PDS system.

3.3.4. Effect of co-existing ions. Halide ions (Cl^- and F^-) are often found in surface water, groundwater, or seawater in the concentration range of 0.1–500 mg L^{-1}. These halide ions undergo photo excitation on UV exposure and produce radicals that selectively degrade pollutants. Additionally, these ions also act as $^{\bullet}OH$ scavengers, thereby decreasing the $^{\bullet}OH$ radical-mediated degradation of SA.[59] A correlation between the added Cl^- ion and SA degradation rate was obtained for the experiment (Fig. S3a†). When the Cl^- concentration increased from 5 to 15 mM, the SA degradation was slightly enhanced from 52.24 ± 0.66% to 66.87 ± 0.45%, which might be due to the interaction between the $SO_4^{\bullet-}$ and Cl^- to produce the $Cl^{\bullet}$ radical with a high redox potential of 2.40 V and degrade SA further. However, the overall SA degradation rate decreased from 0.017 ± 0.001 min^{-1} to 0.004 ± 0.0002 min^{-1} in the presence of Cl^-, which is attributed to the reaction between the Cl^- and $^{\bullet}OH$ (2.80 V) that produced comparatively fewer active oxidants such as $ClOH^{\bullet-}$, $Cl^{\bullet}$, and $Cl_2^{\bullet-}$ (eqn (12)–(16)), thus lowering the degradation efficiency in the UV/PDS/Zn–Al@HC system on Cl^- exposure.

A similar trend was also observed earlier for acetaminophen and trichloroethylene degradation by the UV/PDS system,[60,61] whereas the presence of F^- ion enhanced the SA degradation rate maximum up to 0.025 min^{-1} at a F^- concentration of 15 mM (removal efficiency of 97.29 ± 0.55%). However, the results showed an inhibitory effect of F^- at a concentration of 10 mM. The SA degradation efficiency was 67.75 ± 0.50% for 5 mM and 84.55 ± 0.61% for 10 mM concentration of F^- ion (Fig. S3b†). Hence, F^- ion had a two-sided effect (both positive and negative) on the SA degradation in the UV/PDS/Zn–Al@HC system.

$$Cl^- + {}^{\bullet}OH/SO_4^{\bullet-} \rightarrow ClOH^{\bullet-}/SO_4^{2-}/Cl^{\bullet} \quad (12)$$

$$Cl^{\bullet} + Cl^- \rightarrow Cl_2^{\bullet-} \quad (13)$$

$$Cl^{\bullet} + H_2O \rightarrow ClOH^{\bullet-} + H^+ \quad (14)$$

$$2Cl^- + Zn\text{–}Al@HC\ (h_{VB}^+) \rightarrow Cl_2 \quad (15)$$

$$S_2O_8^{2-} + 2Cl^- \rightarrow 2SO_4^{2-} + Cl_2 \quad (16)$$

The effect of NO_3^- on the photocatalytic degradation of SA is provided in Fig. S3c.† The addition of a low dosage of NO_3^- had an inhibitory effect on the SA degradation and decreased the degradation efficiency of SA. On comparing with the NO_3^- free system having an SA degradation rate of 0.017 min^{-1} (NO_3^- = 0 mM), the degradation rate reduced to 0.0074 min^{-1} (for 5 mM), 0.0071 min^{-1} (for 10 mM), and 0.009 min^{-1} (for 15 mM). The negative effect of NO_3^- is attributed to the radical scavenging properties of NO_3^-, which reacts with the $^{\bullet}OH$ and the h^+ (eqn (17) and (18)). The results obtained are consistent with the previous investigation performed on the photocatalytic degradation of carbamazepine.[62]

$$NO_3^- + h^+ \rightarrow NO_3^{\bullet} \quad (17)$$

$$NO_3^- + {}^{\bullet}OH \rightarrow NO_3^{\bullet} + OH^- \quad (18)$$

A slight suppression in the SA degradation was observed (Fig. S3d†) in the case of CO_3^{2-} addition, possibly due to the conversion of CO_3^{2-} to HCO_3^- on reaction with water (eqn (19)). Both CO_3^{2-} and HCO_3^- compete for the radical species $^{\bullet}OH$ and $SO_4^{\bullet-}$ to produce less reactive radical moieties $CO_3^{\bullet-}$ and $HCO_3^{\bullet}$.[63] Previous investigations reported the same trend concerning the CO_3^{2-} ion on the carbamazepine degradation in the thermally activated PDS system.[64]

$$CO_3^{2-} + H_2O \rightarrow HCO_3^- + OH^- \quad (19)$$

In the presence of phosphate ions in the aqueous phase, an accelerating effect on SA degradation was noticed. Enhanced degradation efficiencies of 95.03 ± 0.84%, 99.95 ± 0.02%, and 99.96 ± 0.01% were observed at 5, 10, and 15 mM of PO_4^{3-}, respectively (Fig. S3e†). This can be attributed to the adsorption of PO_4^{3-} on the Zn–Al@HC surface which promotes e^-–h^+ separation *via* inducing an electrostatic field on the Zn–Al@HC surface, therefore enhancing the photocatalytic degradation of SA.[59] As shown in Fig. S4a–e,† the effect of anions on the UV/PDS/Zn–Al@HC revealed that Cl^- had the most inhibitory effects on SA degradation in the concentration range of 5–15 mM, followed by NO_3^-, CO_3^{2-}, F^-, and PO_4^{3-} ($Cl^- > NO_3^- > CO_3^{2-} > F^- > PO_4^{3-}$).

3.3.5. Effect of an aqueous matrix and residual sulphate. The synchronous decay of SA by the UV/PDS/Zn–Al@HC system was evaluated (Fig. S5a and b†) in three different types of aqueous matrixes including distilled water, tap water, and secondary treated sewage (WWTP effluent). The results are thoroughly explained in Text S4.†

3.4. Identification of the predominant radical species

To elucidate the effect of different radical species involved in the UV/PDS/Zn–Al@HC system on SA degradation, a scavenging experiment using TBA and MeOH was conducted. MeOH could rapidly react with both $^{\bullet}OH$ ($k = 9.7 \times 10^8$ M^{-1} s^{-1}) and $SO_4^{\bullet-}$ ($k = 1.1 \times 10^7$ M^{-1} s^{-1}); whereas, TBA could scavenge $^{\bullet}OH$ radical with the reaction rate constant of $k = 6.0 \times 10^8$ M^{-1} s^{-1}, but not $SO_4^{\bullet-}$ having $k = 4.0 \times 10^5$ M^{-1} s^{-1}.[65] The addition of TBA at the concentration of 50 mM to the UV/PDS/Zn–Al@HC system decreased the degradation efficiency from 94.45 ± 0.65% to 41.22 ± 0.15%, which shows the dominancy of $^{\bullet}OH$ in the SA degradation (Fig. 7a and b).

The SA degradation in the TBA exposed system might be mainly due to the photolysis and activity of $SO_4^{\bullet-}$ in the system. Furthermore, the exposure of MeOH at the same concentration lowers the degradation rate to 25 ± 0.45%, confirming the co-

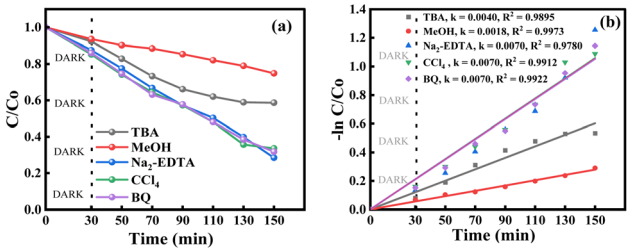

Fig. 7 (a) Scavenging effect of TBA, MeOH, Na_2-EDTA, CCl_4, and BQ on SA decay and (b) kinetics in the UV/PDS/Zn–Al@HC system.

existence and significant contribution of $SO_4^{\bullet-}$ in the UV/PDS/Zn–Al@HC system. In addition, BQ, Na_2-EDTA, and CCl_4 were employed to identify the $O_2^{\bullet-}$, h^+, and e^-, respectively.[66] Furthermore, in the presence of BQ, Na_2-EDTA, and CCl_4, SA degradation was suppressed to 68.15%, 71.48%, and 66.35% in 150 min, respectively. Therefore, the aforementioned results confirmed that both $^{\bullet}OH$ and $SO_4^{\bullet-}$ generated by stimulating PDS in the presence of Zn–Al@HC and UV light played vital roles in the degradation of SA (eqn (7) and 8); however, the role of $O_2^{\bullet-}$, h^+, and e^- also cannot be neglected. Overall, $^{\bullet}OH$ was identified as the principal radical responsible for the abatement of SA in the UV/PDS/Zn–Al@HC system. To validate the involvement of reactive oxygen species in the process, an EPR analysis was performed at room temperature using a 100 mM solution of the DMPO spin-trapping agent. DMPO reacts with short-lived radicals generated in the Zn–Al@HC/PDS system to form stable adducts, which have extended lifespans (eqn (20)–(22)). Clearly, Fig. 8a does not show any peak in the spectrum, thereby revealing no formation of reactive oxygen species in the blank solution, whereas the EPR spectrum of pure PDS revealed sharp peaks (indicated by a star mark) in the spectra of the DMPO–PDS system, which is attributed to the nitroxide radical (5,5-dimethylpyrrolidone-(2)-oxyl-(1); DMPOX) formed as a result of the oxidation of DMPO (Fig. 8b). This observation was consistent with the results of control experiments. However, the distinctly higher peaks of DMPO-$^{\bullet}OH$ with wave intensity of 1 : 2 : 2 : 1, displayed by the Zn–Al@HC/PDS system, signify the accelerated activity of the catalyst towards $^{\bullet}OH$ generation (Fig. 8c),[67] while the minor peaks of DMPO-$SO_4^{\bullet-}$ with the wave intensity of 1 : 1 : 1 support the co-existence of the $SO_4^{\bullet-}$ radical.[67] Hence, the major role of $^{\bullet}OH$ was affirmed by both the scavenging and EPR experiments.

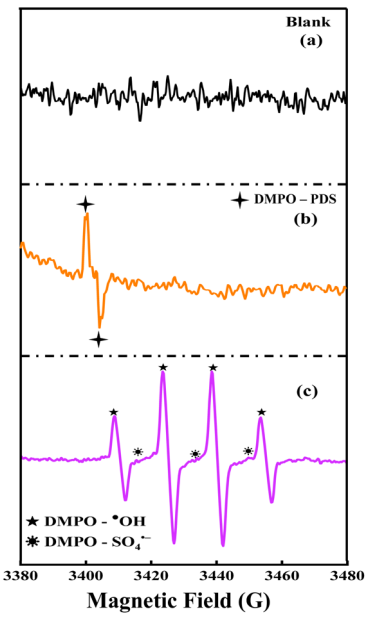

Fig. 8 EPR (a), blank (b), DMPO-PDS (c), DMPO-$^{\bullet}OH$/$SO_4^{\bullet-}$ for the PDS activated Zn–Al@HC photocatalyst.

$$DMPO + SO_4^{\bullet-} \rightarrow DMPO\text{-}SO_4^{\bullet-} \quad (20)$$

$$DMPO\text{-}SO_4^{\bullet-} + H_2O \rightarrow DMPO\text{-}HO^{\bullet} + h^+ + SO_4^{2-} \quad (21)$$

$$DMPO\text{-}HO^{\bullet} \rightarrow Product \quad (22)$$

3.5. Catalytic mechanism involved in the use of the UV/PDS/Zn–Al@HC system

Based on the scavenging experiment and detected free radicals, the mechanism involved in the UV/PDS/Zn–Al@HC system for activating PDS by Zn–Al@HC and further SA degradation is proposed in Fig. 9. Initially, the adsorption mechanism is caused by the capturing of both SA and PDS on the Zn–Al@HC surface and generation of photogenerated e^- and h^+ (eqn (23) and (24)). However, the process of photocatalytic degradation occurred both on the catalyst surface and aqueous media simultaneously. During the process, the dominant $^{\bullet}OH$ radical can be produced in several ways, including the reaction of photogenerated h^+ with the OH^- and H_2O molecules (eqn (26)–(28)), the reaction between $O_2^{\bullet-}$ and H_2O molecules (eqn (25); (29) and (30)), and the reaction of $SO_4^{\bullet-}$ with OH^- and H_2O molecules according to eqn (31) and (32), and eqn (8).[42,68]

Furthermore, the photocatalyst Zn–Al@HC tentatively contributed to the generation of *in situ* H_2O_2 which further releases $^{\bullet}OH$ (eqn (33)–(35)) for contaminant degradation confirming the abundance of $^{\bullet}OH$ during the EPR.

$$ZnAl_2O_4\ (e_{CB}^-) + ZnAl_2O_4\ (h_{VB}^+) \rightarrow 2ZnAl_2O_4\ (e^- – h^+) \quad (23)$$

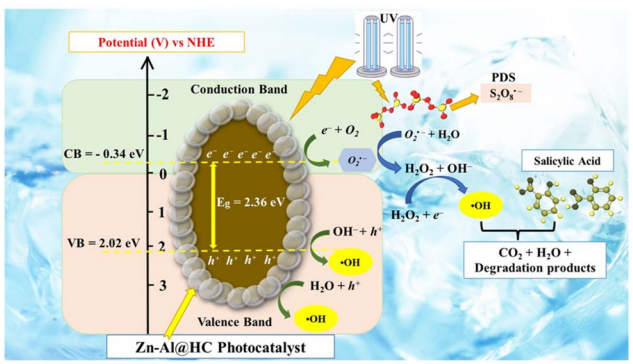

Fig. 9 Proposed photocatalytic mechanism of Zn–Al@HC for reactive radical generation, PDS activation, and SA degradation.

$$\text{Zn–Al@HC } (e_{CB}^-) \rightarrow \text{HC } (e^-) - ZnAl_2O_4 \quad (24)$$

$$\text{HC } (e^-) + O_2 \rightarrow O_2^{\cdot -} \quad (25)$$

$$OH^- + h^+ \rightarrow {}^{\cdot}OH \quad (26)$$

$$H_2O + h^+ \rightarrow {}^{\cdot}OH + H^+ \quad (27)$$

$$H_2O + e^- \rightarrow OH^- + H^+ \quad (28)$$

$$\text{Zn–Al@HC } (e_{CB}^-) + O_2 \rightarrow O_2^{\cdot -} \quad (29)$$

$$O_2^{\cdot -} + 2H_2O \rightarrow H_2O_2 + 2OH^- \rightarrow 2H_2O_2 + e^- \rightarrow 2{}^{\cdot}OH + 2OH^- \quad (30)$$

$$SO_4^{\cdot -} + OH^- \rightarrow {}^{\cdot}OH + SO_4^{2-} \quad (31)$$

$${}^{\cdot}OH/SO_4^{\cdot -} + \text{SA} \rightarrow CO_2 + H_2O + \text{Degradation products} \quad (32)$$

$$2H_2O \rightarrow H_2O_2 + 2\,(H^+ + e^-) \quad (33)$$

$$H_2O_2 + h\nu \rightarrow 2{}^{\cdot}OH \quad (34)$$

$$\text{PFR/HC} + H_2O_2 \rightarrow 2{}^{\cdot}OH \quad (35)$$

On the other hand, the probable generation of $SO_4^{\cdot -}$ can take place *via* either photodecomposition of PDS by UV light (eqn (36)), or activation of PDS by the HC-based catalyst *via* an e^- transfer mechanism (eqn (37)–(39)), or reaction between PDS and photogenerated e^- (eqn (7)). Both the generated radicals attack the SA molecules and photocatalytically degrade to intermediates and then to CO_2 and H_2O on further oxidation (eqn (32)).[69]

$$S_2O_8^{2-} + h\nu \rightarrow 2SO_4^{\cdot -} \quad (36)$$

$$S_2O_8^{2-} + \text{HC surface–COOH} \rightarrow SO_4^{\cdot -} + HSO_4^- + \text{HC surface–COO}^{\cdot} \quad (37)$$

$$S_2O_8^{2-} + \text{HC surface–OH} \rightarrow SO_4^{\cdot -} + HSO_4^- + \text{HC surface–O}^{\cdot} \quad (38)$$

$$S_2O_8^{2-} + \text{HC surface–C=O} \rightarrow SO_4^{\cdot -} + SO_4^{2-} + \text{HC surface–CO}^{\cdot} \quad (39)$$

3.6. Mineralisation sequence, evolution of oxidation products, and total organic carbon removal during SA degradation in the UV/PDS/Zn–Al@HC system

From the inference of the Liquid Chromatograph Mass-Spectroscopy (LC-MS) analysis (as shown in Fig. S6†) of the initial and final treated sample taken under optimum conditions, a plausible reaction pathway for the SA mineralization and intermediate formation is proposed in Fig. 10. As per the results, oxidative degradation of SA started with the attack of ·OH radical on SA, leading to the formation of polyhydroxylated benzene derivatives, such as 2,3-dihydroxybenzoic, 2,5-dihydroxybenzoic, and 2,6-dihydroxybenzoic acids.[70]

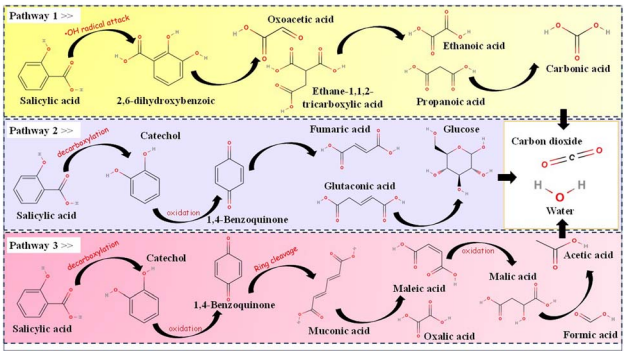

Fig. 10 Proposed degradation pathway for the photocatalytic degradation of SA by the Zn–Al@HC photocatalyst in the UV/PDS system.

Simultaneously, the decarboxylation of SA resulted in the formation of catechol and it further oxidized to form 1,2-benzoquinone.[71] The cleavage of the benzene ring of 1,2-benzoquinone in the aqueous medium gives rise to aliphatic carboxylic acids, such as muconic acid. Maleic acid and oxalic acids are formed by the addition of ·OH to the double bond of the muconic acid. Then maleic acid was oxidized to malic acid and further decomposed to acetic acid and CO_2. On the other hand, the generated oxalic acid transformed into formic acid and then to CO_2.[72] The *p*-position of the C=O groups initiated an attack on 1,2-benzoquinone, leading to the formation of H_2O_2 intermediates. These intermediates subsequently converted into 2-hydroxy-1,4-benzoquinone through the release of water. 2-Hydroxy-1,4-benzoquinone was oxidized to fumaric acid, caffeic acid, glutaconic acid, and other small molecules such as glucose and fructose.[73]

Furthermore, 2,3-dihydroxybenzoic acid was oxidized to oxoacetic acid and ethane-1,1,2- tricarboxylic acid. These compounds are further converted to ethanoic acid and propanoic acid. Then, propanoic acid was oxidized to carbonic and hydroxyl acetic acid. Subsequently, hydroxyl acetic acid was again converted to ethanoic and carbonic acids, which directly mineralised to CO_2 and H_2O.[74] The degradation products and intermediates formed with their respective *m*/*z* values are listed in Table S2.†

Despite the high SA degradation rate obtained in the present experiment, SA was not completely mineralized to CO_2 and H_2O. There might be the formation of the above discussed organic by-products, which might be toxic to aquatic and terrestrial systems. To better evaluate the final organic concentration, the total organic carbon (TOC) was determined at each designated sampling time for the system having an initial concentration of SA = 50 mg L^{-1}, PDS = 0.01 M, and Zn–Al@HC = 10 mg L^{-1}. Results showed a drastic decrease in TOC content, and a maximum of 85.21 ± 1.25% of TOC removal efficiency was achieved after 360 min. Similar results were obtained by Shinde *et al.* and Garza-Campos *et al.* with a TOC abatement efficiency of 88.9% and 87%, respectively, during the photocatalytic degradation of SA by deploying $TiO_2/AlFe_2O_3$ as the

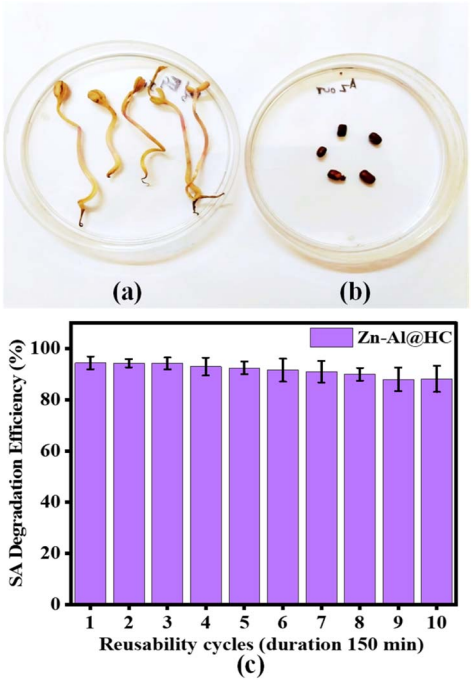

Fig. 11 Evaluation of *Vigna radiata* germination on exposure to (a) treated and (b) untreated wastewater sample; (c) reusability assessment of Zn–Al@HC.

photocatalyst and coupling a solar photoelectron-Fenton-solar heterogeneous photocatalysis system.[75,76]

Finally, phytotoxicity evaluation was performed against *Vigna radiata* because of its rapid germination, low-cost, and highly sensitive nature to scrutinize the toxicity of the treated sample (containing transitional intermediates). The results showed significant growth of roots up to 1 ± 0.5 cm and shoots up to 6 ± 0.9 cm in the treated sample that contained 2.7 mg L^{-1} of SA after eliminating 94.45 ± 0.65% of SA under optimum conditions for twelve days (Fig. 11a and b). However, no growth of *Vigna radiata* was observed on exposure to the untreated sample having 50 mg L^{-1} of SA. The results emphasised the degradation of SA into less toxic products during the UV/PDS/Zn–Al@HC treatment and intermediates (hydroxylated compounds) have a low inhibitory effect and the phytotoxicity decreased. The past investigations discovered that the untreated SA solution hindered the germination and lengthening of the root and shoot of *Vigna radiata* and *Vicia faba*.[77,78] Additionally, the results demonstrated that SA concentrations of 3.95 and 4.16 mg L^{-1} remained after the electrocoagulation, and electro-Fenton treatments showed significant germination and elongation of seeds.[77,78] Thus, the treated effluent can be reliably utilized for irrigation, gardening, and other recreational purposes.

Furthermore, the reusability assessment of Zn–Al@HC revealed the outstanding performance of the catalyst for 10 continuous cycles (Fig. 11c) under optimized conditions, which was also demonstrated by the 20 cycles CV mentioned earlier. Results of the reusability test revealed that the SA degradation dropped to 88 ± 0.5% after the 9th successive cycle from 94.45 ± 0.65% (1st cycle), with maximum Al and Zn leaching of 1.2 ± 0.2 mg L^{-1} and 0.6 ± 0.1 mg L^{-1}, respectively, which is significantly less than the United States, Environmental Protection Agency (US-EPA) guidelines (Al <5.0 mg L^{-1}, and Zn <2.0 mg L^{-1}) for irrigation,[79,80] thus revealing the excellent potency of the catalyst even after 9 cycles of reuse. After usage, Zn–Al@HC was regenerated using alkali EtOH to enhance the sustainability of the catalyst, and nearly 90 ± 0.5% SA degradation efficiency was achieved after regeneration.

3.7. Cost and performance assessment

The photodegradation of SA by one order of magnitude in 1 m^3 of wastewater in the photochemical process utilizes a significant amount of electrical energy and oxidants, thereby raising the total operational cost of the UV/PDS system. Thus, electrical energy per order (EE_{UV}), total oxidant consumed (ox), and their corresponding $Cost_{UV}$ and $Cost_{OX}$ for batch reactions can be estimated using eqn (40)–(43), respectively.

$$EE_{UV}(\text{kW h m}^{-3}\text{per order}) = \frac{I \times t \times A}{V \times \log\left(\frac{C_o}{C_t}\right)} \quad (40)$$

$$\text{Cost}_{UV}(\$\ \text{per m}^{-3}) = EE_{UV}\ (\text{kW h m}^{-3}\ \text{order}^{-1}) \times \text{electricity cost}\ (\$\ \text{per kW h}^{-1}) \quad (41)$$

$$\text{Cost}_{OX}(\$\ \text{per m}^3) = \frac{\text{Total oxidant consumed} \times \text{oxidant cos}\, t}{V} \quad (42)$$

The total operating cost ($Cost_{total}$) of the system can be estimated using eqn (43).

$$\text{Cost}_{total}\ (\$\ \text{per m}^{-3}) = \text{Cost}_{UV} + \text{Cost}_{OX} \quad (43)$$

Herein, EE_{UV} is the electrical energy per order (kW h m^{-3} $order^{-1}$), I represents the light intensity input to the photochemical system (11 μW cm^{-2}), t signifies the reaction duration (150 min), V is the volume of liquid in the system (1 L), A is the surface area of water receiving the UV irradiation (cm^2), and C_0 and C_t are the initial and ultimate amounts of SA (mg L^{-1}), respectively. The cost of electricity and PDS were considered to be $ 0.1 per kW h and $ 0.064 per kg, respectively, as per Indian market cost.[81]

Under the optimal experimental conditions of 50 mg L^{-1} of SA, 10 mg L^{-1} of Zn–Al@HC, PDS dosage of 0.01 M, and UV irradiation of 11 μW cm^{-2}, UV/PDS/Zn–Al@HC consumed 0.013 kW h m^{-3} $order^{-1}$ of EE_{UV}, which was about 345, 2223, and 6686 folds lower than those of UV/PDS, Zn–Al@HC/UV, and Zn–Al@HC/PDS, respectively (Table 1). Similarly, the $Cost_{total}$ of UV/PDS/Zn–Al@HC was estimated at 0.1536 $ per m^{-3} $order^{-1}$ to achieve 94.45 ± 0.65% degradation of SA. The lowered EE_{UV} and $Cost_{total}$ of UV/PDS/Zn–Al@HC shows that higher pollutant elimination can result in lower energy consumption and operating costs.

An earlier investigation on the degradation of SA using an electro-Fenton system consumed 0.171 kW h m^{-3} $order^{-1}$ of EE_o and 0.22 $ m^{-3} to obtain 91.68% degradation of 50 mg L^{-1}

Table 1 Cost assessment of UV/PDS/Zn–Al@HC, UV/PDS, Zn–Al@HC/PDS, and Zn–Al@HC/UV for the degradation of SA

Degradation process	UV/PDS/Zn–Al@HC	UV/PDS	Zn–Al@HC/UV	Zn–Al@HC/PDS
EE_{UV} (kW h m^{-3} $order^{-1}$)	0.0130	4.4879	28.8975	86.9246
$Cost_{UV}$ (\$ per m^{-3})	0.0013	0.4488	3.4677	8.6925
$Cost_{ox}$ (\$ per m^{-3})	0.1523	0.1523	0.1523	0.1523
$Cost_{total}$ (\$ per m^{-3})	0.1536	0.6011	3.6200	8.8448
$Cost_{total}$ (Rs per m^{-3})	12.6828	49.6235	298.8338	730.1381

of SA.[77] Similarly, another investigation demonstrated the degradation of 50 mg L^{-1} of SA by 69.5% within 100 min at a pH of 3.0, requiring 11.91 kW h m^{-3} of electrical energy in the peroxi-coagulation process.[2] Thus, compared to the earlier investigations, UV/PDS/Zn–Al@HC required considerably less electrical energy and operating cost, making it a more cost-effective treatment as an alternative for treating SA-laden wastewater. Few other investigations have also adopted different cost-effective methods to treat SA, which are summarised in Table S3.†

4. Conclusions

The present research claimed the efficacious valorisation of AD-FW using HTC for the synthesis of an economic and highly efficient Zn–Al-based photocatalyst. The novel composite of a Zn and Al precursor with the HC resulted in enhanced photocatalytic and electrochemical properties of the synthesized catalyst (Zn–Al@HC) compared to the pristine HC. Zn–Al@HC decomposed PDS to reactive radicals *via* UV irradiation, and established about 94.45 ± 0.65% degradation of the model pollutant SA in the setup under optimum operating conditions (Zn–Al@HC = 10 mg L^{-1}, PDS = 0.01 M, SA = 50 mg L^{-1}). An increment in the catalyst and PDS dosage had a positive correlation with the SA degradation rate. Despite the scavenging effect of anions Cl^-, NO_3^-, and CO_3^{2-}, SA degradation efficiencies of 66.87 ± 0.45%, 74.67 ± 0.60%, and 88.64 ± 0.10% were achieved, which highlighted the potent applicability of Zn–Al@HC under harsh conditions. In contrast, the exposure to anions F^- and PO_4^{3-} showed excellent SA degradation with more than 99% efficiency. Moreover, Zn–Al@HC showed satisfactory performance in real wastewater with an SA abatement efficiency of 78.19 ± 0.10%. Furthermore, the catalyst was found to be highly stable as demonstrated by 20 cycles of CV analysis. The EE_{UV} and $Cost_{total}$ of the UV/PDS/Zn–Al@HC system were 0.0130 kW h m^{-3} $order^{-1}$ and 0.1536 \$ per m^{-3} $order^{-1}$, which evidenced the cost-effectiveness of the UV/PDS/Zn–Al@HC system compared to the other reported photocatalytic degradation systems for SA. Thus, the suggested treatment system can be implemented at the pilot or field-scale at the tertiary stage in WWTPs and can be explored for other organic CECs in the future.

5. Environmental implications

SA is extensively utilized in the production of pharmaceuticals, cosmetics, antipyretics, and painkillers. However, it causes environmental hazards due to its high toxicity, endocrine disrupting properties, non-biodegradability, and tendency to accumulate in the ecosystem. Conventional WWTPs of the industrial sector struggle to eliminate CECs from contaminated water due to their non-biodegradable nature. To address this challenge, photocatalysis systems have emerged as promising advanced tertiary treatment methods and can be added as a downstream process to any biological unit in conventional WWTPs. Photocatalysis systems offer advantages such as high degradation rates, operational simplicity, and shorter processing times. In this context, deriving photocatalysts from AD-FW can solve multiple environmental issues, such as inappropriate FW management, AD management, less waste to landfill, carbon emission and severe health hazards due to the unscientific disposal of hazardous waste.

Similarly, in an attempt to extend the scope of the procedure, metals (Zn and Al) used for photocatalyst synthesis at a large scale could also be derived from industrial waste including electroplating residues, zinc batteries, spent aluminium cans, *etc.* targeting the other solid waste stream (E-waste). Hence, the present novel material Zn–Al@HC photocatalyst could be a game-changing solution to reduce environmental pollution, support the concept of circular economy (Fig. 12), and promote environmental sustainability at a relatively lower cost.

5.1. Novelty statement

For the first time, an AD-FW derived photocatalyst (Zn–Al@HC) synthesized using a greener approach (one-pot method, lower energy requirements, and waste-derived precursor) is utilized for remediation of SA from wastewater. Also, process optimization under diverse operating conditions and real environment application is thoroughly discussed in the present

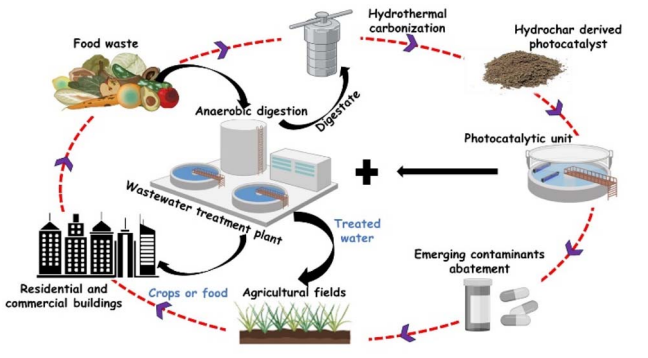

Fig. 12 Proposed field scale Zn–Al@HC implementation scheme for pollution abatement, reducing energy requirement, and environmental sustainability.

investigation, *i.e.*, unique from previous investigations. Additionally, waste-derived catalysts cut back the cost of utilizing commercial expensive catalysts and can offer the photocatalysis technology at an affordable cost and enhance the sustainability.

Author contributions

Shraddha Yadav: conceptualization, formal analysis, investigation, methodology, writing – original draft; writing – review & editing. Monali Priyadarshini: validation, visualization, writing – original draft, data curation, writing – review & editing, investigation. Azhan Ahmad: software, visualization, writing – original draft, writing –review & editing. Makarand M. Ghangrekar: funding acquisition, project administration, resources, supervision, validation, writing – review & editing. Brajesh K. Dubey: resources, supervision, validation, writing – review & editing.

Conflicts of interest

The authors declare that they have no known competing financial interests or personal relationships that could have appeared to influence the work reported in this paper.

Acknowledgements

The current research work is funded by a research grant from the Department of Science and Technology, Government of India (File no.: DST/TMD (EWO)/OWUIS-2018/RS-10).

Notes and references

1 Y. Liu, Y. Sun and Z. Peng, *Desalination*, 2022, **537**, 115866.
2 İ. Y. Köktaş and Ö. Gökkuş, *Chemosphere*, 2022, **293**, 133566.
3 A. Adak, I. Das, B. Mondal, S. Koner, P. Datta and L. Blaney, *Emerging Contam.*, 2019, **5**, 53–60.
4 A. Huang, D. Zhi and Y. Zhou, *Environ. Pollut.*, 2021, **286**, 117310.
5 M. Priyadarshini, I. Das, M. M. Ghangrekar and L. Blaney, *J. Environ. Manage.*, 2022, **316**, 115295.
6 O. K. Türk, G. Adalar, S. Yazici Guvenc, E. Can-Güven, G. Varank and A. Demir, *Environ. Sci. Pollut. Res.*, 2023, **30**, 869–883.
7 H. Xu, T. Zhang, D. Wang, D. Cai, S. Chen, H. Wang, S. Shu and Y. Zhu, *Sep. Purif. Technol.*, 2022, **300**, 121833.
8 V. M. Daskalaki, M. Antoniadou, G. Li Puma, D. I. Kondarides and P. Lianos, *Environ. Sci. Technol.*, 2010, **44**, 7200–7205.
9 M. Mitra, A. Ghosh, A. Mondal, K. Kargupta, S. Ganguly and D. Banerjee, *Appl. Surf. Sci.*, 2017, **402**, 418–428.
10 F. Wang, Y. Liu, M. Cao, B. Zhou, H. Chen, R. Yuan, S. Liu and B. Xing, *Environ. Sci. Technol.*, 2023, **57**, 3691–3702.
11 U. P. S. Gahlaut, V. Kumar and Y. C. Goswami, *Phys. E*, 2020, **117**, 113792.
12 X. H. Yi, H. Ji, C. C. Wang, Y. Li, Y. H. Li, C. Zhao, A. Wang, H. Fu, P. Wang, X. Zhao and W. Liu, *Appl. Catal., B*, 2021, **293**, 120229.
13 X. H. Yi, T. Y. Wang, H. Y. Chu, Y. Gao, C. C. Wang, Y. J. Li, L. Chen, P. Wang, H. Fu, C. Zhao and W. Liu, *Chem. Eng. J.*, 2022, **449**, 137784.
14 S. Yadav, A. Ahmad, M. Priyadarshini, B. K. Dubey and M. Ghangrekar, *FlatChem*, 2024, **44**, 100623.
15 J. Wei, Y. Liu, Y. Zhu and J. Li, *Chemosphere*, 2020, **247**, 125854.
16 U. M. García-Pérez, A. Martínez-De La Cruz and J. Peral, *Electrochim. Acta*, 2012, **81**, 227–232.
17 X. Li, T. Wan, J. Qiu, H. Wei, F. Qin, Y. Wang, Y. Liao, Z. Huang and X. Tan, *Appl. Catal., B*, 2017, **217**, 591–602.
18 U. Ghosh and A. Pal, *J. Water Process Eng.*, 2022, **50**, 103315.
19 S. Krishnan and A. Shriwastav, *Environ. Res.*, 2023, **216**, 114568.
20 A. Kamal, U. Haroon, H. Manghwar, K. H. Alamer, I. M. Alsudays, A. T. Althobaiti, A. Iqbal, M. Akbar, M. Anar and M. Nazish, *Molecules*, 2022, **27**, 5333.
21 H. B. Sharma and B. K. Dubey, *Waste Manage.*, 2020, **118**, 521–533.
22 S. Soltani, U. Rashid, R. Yunus and Y. H. Taufiq-Yap, *Fuel*, 2016, **178**, 253–262.
23 A. Chaudhary, A. Mohammad and S. M. Mobin, *Mater. Sci. Eng., B*, 2018, **227**, 136–144.
24 A. Elhalil, R. Elmoubarki, A. Machrouhi, M. Sadiq, M. Abdennouri, S. Qourzal and N. Barka, *J. Environ. Chem. Eng.*, 2017, **5**, 3719–3726.
25 Z. Huang, L. Shi, Y. Muhammad and L. Li, *J. Colloid Interface Sci.*, 2021, **586**, 423–432.
26 L. Yang, H. Wang, J. Sun, Y. Xu, P. Li, Y. Xu and S. Wu, *IET Renew. Power Gener.*, 2021, **15**, 1397–1407.
27 Z. Chen, H. Jia, Y. Guo, Y. Li and Z. Liu, *Environ. Res.*, 2022, **208**, 112695.
28 S. Siara, C. Elvis, R. Harishkumar and P. Velayudhaperumal Chellam, *Mater. Res. Bull.*, 2022, **145**, 111530.
29 S. Masoumi and A. K. Dalai, *J. Cleaner Prod.*, 2020, **263**, 121427.
30 Q. Li, G. Wei, Y. Yang, Z. Li, L. Zhang and Q. Huang, *J. Hazard. Mater.*, 2020, **394**, 122566.
31 P. Zhang, R. Y. Hong, Q. Chen and W. G. Feng, *Powder Technol.*, 2014, **253**, 360–367.
32 X. Zhu, Y. Liu, F. Qian, Z. Lei, Z. Zhang, S. Zhang, J. Chen and Z. J. Ren, *Environ. Sci. Technol.*, 2017, **51**, 10756–10764.
33 J. T. Titantah and D. Lamoen, *Diam. Relat. Mater.*, 2007, **16**, 581–588.
34 L. Jiang, X. Yuan, Y. Pan, J. Liang, G. Zeng, Z. Wu and H. Wang, *Appl. Catal., B*, 2017, **217**, 388–406.
35 Z. Zhang, Z. Hua, J. Lang, Y. Song, Q. Zhang, Q. Han, H. Fan, M. Gao, X. Li and J. Yang, *CrystEngComm*, 2019, **21**, 4607–4619.
36 S. Biswas, H. Siddiqi, B. C. Meikap, T. K. Sen and M. Khiadani, *Water, Air, Soil Pollut.*, 2020, **231**(3).
37 S. Sutar, S. Otari and J. Jadhav, *Chemosphere*, 2022, **287**, 132200.
38 M. Ramani, S. Ponnusamy and C. Muthamizhchelvan, *Opt. Mater.*, 2012, **34**, 817–820.
39 S. Suwanboon, P. Amornpitoksuk, T. Rattana and C. Randorn, *Ceram. Int.*, 2020, **46**, 21958–21977.

40 K. V. Kumar and S. D. Bhavani, *East Eur. J. Phys.*, 2023, **2023**, 355–362.
41 K. Guan, P. Zhou, J. Zhang and L. Zhu, *J. Mol. Struct.*, 2020, **1203**, 127425.
42 M. Amir, T. Fazal, J. Iqbal, A. A. Din, A. Ahmed, A. Ali, A. Razzaq, Z. Ali, M. S. U. Rehman and Y. K. Park, *J. Ind. Eng. Chem.*, 2022, **115**, 171–182.
43 N. Iqbal, *J. Photochem. Photobiol., A*, 2022, **427**, 113813.
44 D. Roy, S. Neogi and S. De, *Chem. Eng. J.*, 2022, **430**, 133069.
45 J. Liu, J. Ma, X. Du, F. Han, S. Shi and G. Yang, *J. Alloys Compd.*, 2021, **862**, 158017.
46 A. K. Dey, S. R. Mishra and M. Ahmaruzzaman, *Environ. Sci. Pollut. Res.*, 2023, **30**, 53887–53903.
47 X. An, Y. Chen, M. Ao, Y. Jin, L. Zhan, B. Yu, Z. Wu and P. Jiang, *Chem. Eng. J.*, 2022, **435**, 135087.
48 D. C. Madu, S. M. Islam, H. Pan and C. J. Barile, *J. Mater. Chem. C*, 2021, **9**, 6297–6307.
49 Y. Nosaka and A. Nosaka, *ACS Energy Lett.*, 2016, **1**, 356–359.
50 X. Shi, S. Back, T. M. Gill, S. Siahrostami and X. Zheng, *Chem*, 2021, **7**, 38–63.
51 A. Fernandes, M. J. Nunes, A. S. Rodrigues, M. J. Pacheco, L. Ciríaco and A. Lopes, *Molecules*, 2021, **26**, 4821.
52 Y. Liang, Z. Zeng, J. Yang, G. Yang and Y. Han, *Colloids Surf., A*, 2021, **624**, 126796.
53 Z. Guo, M. Deng, H. Wang, X. Xiang, C. Zhang and B. Wang, *J. Phys. Chem. Solids*, 2024, **185**, 111729.
54 B. Sun, H. Li, Q. Wei, S. Xue, A. Zhou and X. Yue, *Sep. Purif. Technol.*, 2022, **301**, 122039.
55 H. Heidarpour, M. Padervand, M. Soltanieh and M. Vossoughi, *Chem. Eng. Res. Des.*, 2020, **153**, 709–720.
56 R. Li, H. Hu, Y. Ma, X. Liu, L. Zhang, S. Zhou, B. Deng, H. Lin and H. Zhang, *J. Cleaner Prod.*, 2020, **276**, 124246.
57 D. Lambropoulou, E. Evgenidou, V. Saliverou, C. Kosma and I. Konstantinou, *J. Hazard. Mater.*, 2017, **323**, 513–526.
58 S. Bekkouche, S. Merouani, O. Hamdaoui and M. Bouhelassa, *J. Photochem. Photobiol., A*, 2017, **345**, 80–91.
59 A. Tufail, W. E. Price and F. I. Hai, *Membranes*, 2020, **10**, 1–15.
60 C. Tan, N. Gao, S. Zhou, Y. Xiao and Z. Zhuang, *Chem. Eng. J.*, 2014, **253**, 229–236.
61 C. Liang, Z. S. Wang and N. Mohanty, *Sci. Total Environ.*, 2006, **370**, 271–277.
62 X. Gao, Q. Guo, G. Tang, W. Peng, Y. Luo and D. He, *J. Water Reuse Desalin.*, 2019, **9**, 301–309.
63 S. Dhaka, R. Kumar, S. hun Lee, M. B. Kurade and B. H. Jeon, *J. Cleaner Prod.*, 2018, **180**, 505–513.
64 J. Deng, Y. Shao, N. Gao, Y. Deng, S. Zhou and X. Hu, *Chem. Eng. J.*, 2013, **228**, 765–771.
65 C. Tan, D. Fu, N. Gao, Q. Qin, Y. Xu and H. Xiang, *J. Photochem. Photobiol., A*, 2017, **332**, 406–412.
66 M. Abdelbaky, A. M. Abdelghany, A. H. Oraby, E. M. Abdelrazek and M. M. Rashad, *J. Inorg. Organomet. Polym. Mater.*, 2023, **33**, 3304–3314.
67 S. Ding, J. Wan, Y. Wang, Z. Yan and Y. Ma, *Chem. Eng. J.*, 2021, **422**, 130406.
68 M. Sabri, A. Habibi-Yangjeh and S. Vadivel, *Mater. Chem. Phys.*, 2020, **239**, 121988.
69 A. A. Babaei, M. Golshan and B. Kakavandi, *Process Saf. Environ. Prot.*, 2021, **149**, 35–47.
70 E. Guinea, C. Arias, P. L. Cabot, J. A. Garrido, R. M. Rodríguez, F. Centellas and E. Brillas, *Water Res.*, 2008, **42**, 499–511.
71 N. Rabaaoui and M. S. Allagui, *J. Hazard. Mater.*, 2012, **243**, 187–192.
72 J. Wang, M. Xu, X. Liang, Y. Zhang, D. Yang, L. Pan, W. Fang, C. G. Zhu and F. Wang, *Sep. Purif. Technol.*, 2021, **263**, 118368.
73 D. Mukherjee, A. K. Ray and S. Barghi, *Processes*, 2016, **4**, 13.
74 S. J. George, R. Gandhimathi, P. V. Nidheesh and S. T. Ramesh, *Clean: Soil, Air, Water*, 2014, **42**, 1701–1711.
75 S. S. Shinde, C. H. Bhosale and K. Y. Rajpure, *J. Mol. Catal. A: Chem.*, 2011, **347**, 65–72.
76 B. Garza-Campos, E. Brillas, A. Hernández-Ramírez, A. El-Ghenymy, J. L. Guzmán-Mar and E. J. Ruiz-Ruiz, *J. Hazard. Mater.*, 2016, **319**, 34–42.
77 M. Priyadarshini, A. Ahmad and M. M. Ghangrekar, *Environ. Pollut.*, 2023, **322**, 121242.
78 A. Ahmad, M. Priyadarshini, I. Das, M. M. Ghangrekar and R. Y. Surampalli, *J. Environ. Chem. Eng.*, 2023, **11**, 109049.
79 M. of E. and P. British Columbia, *Aluminum Water Quality Guidelines – Wildlife , Livestock Watering , and Irrigation (Reformatted Guideline from 1988)*, Ministry of Water,Land and Resource Stewardship, 1988.
80 M. of E. L. and P. British Columbia, *Ambient Water Quality Guidelines for Zinc. Water Management Branch Ministry of Environment and Climate Change Strategy*, 1999.
81 Y. Zhang, Y. Xiao, Y. Zhong and T. T. Lim, *Chem. Eng. J.*, 2019, **372**, 420–428.